Finite Elements in Analysis and Design 234 (2024) 104128

Contents lists available at ScienceDirect

Finite Elements in Analysis & Design

journal homepage: www.elsevier.com/locate/finel

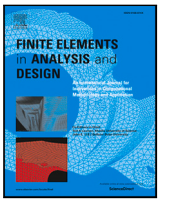

Thermo-mechanical analyses of masonry structures in fire conditions

Daniele Pellegrini

Institute of Information Science and Technologies "A. Faedo", ISTI–CNR, Pisa, Italy

ARTICLE INFO

Keywords:
Masonry structures
Masonry-like material
Nonlinear elasticity
Fire conditions
Thermal loads
Thermal analysis

ABSTRACT

Historic masonry buildings are highly vulnerable to anthropic actions and environmental factors due to their low tensile strength, and bounded compressive strength. Over the years, numerous studies and experimental campaigns have been conducted to characterise the buildings' response to external actions and identify solutions for their conservation against multiple factors, such as climatic changes, material ageing and earthquakes. However, the historic masonry structures' response in case of fire and their safety assessment in post-fire conditions, still needs to be thoroughly investigated both from an experimental and numerical point of view. This paper generalises the constitutive equation of *masonry-like* (or no-tension) materials under non-isothermal conditions to the case in which the masonry has weak tensile strength and bounded compressive strength, even temperature dependent. The generalised constitutive equation is then implemented in NOSA-ITACA and the explicit solution to the equilibrium problem of a masonry circular ring in plane strain condition is calculated and compared with the numerical solution. Subsequently, the code is used to perform an uncoupled thermo-mechanical analysis of a real case study: a masonry barrel vault tested in fire conditions. The agreement between the experimental and numerical results paves the way for further study and research.

1. Introduction

Masonry cultural heritage is an integral part of human history, representing communities' rich architectural traditions and cultural identities worldwide. During their entire life, masonry constructions are constantly threatened by multiple factors, such as climatic changes, ageing of material, earthquakes [1], floods [2], urbanisation [3], and fire [4]; the risk of being lost forever is considerable, and their loss would mean not only a collective history and identity decay but also would have significant socio-economic impacts. While the last decades have witnessed significant developments in the experimental and numerical analysis of the seismic response of historic masonry buildings [5,6], the attention paid to masonry structural response under fire and in post-fire conditions is quite limited. In addition, in Europe, no specific code lays down rules on the fire protection of cultural heritage; only the Recommendation of the European Council no. of 23 November 1993 deals with the safety of cultural assets in a general way, and the [7] provides rules related to the design and safety assessment, in case of fire scenario, of linear elements (walls or slabs) of new construction [8]. Experimental tests on masonry structures under fire are crucial to understand their behaviour and performance during a fire event. In general, they involve a portion [9,10] or full masonry structural elements subjected to controlled fire conditions in a laboratory or on-site environment [11–14]. Their primary objective is to evaluate the response of masonry structures to fire, including their thermal behaviour, structural integrity, and failure mechanisms [8]. Even if different testing procedures and methods are used to evaluate masonry's thermal and mechanical properties, all the documents in the literature [8,12,15–18] show a general decay in these properties with increasing temperature. In particular, the compressive strength that governs the load-bearing

E-mail address: daniele.pellegrini@isti.cnr.it.

https://doi.org/10.1016/j.finel.2024.104128
Received 27 November 2023; Received in revised form 4 February 2024; Accepted 4 February 2024

capacity of fire-exposed components can undergo a reduction of up to 70%–80% due to high temperatures [10,18], while the tensile strength, usually neglected in ambient temperature, can govern the magnitude of spalling and thermally induced cracks [12] but still showing a decrease of up to 80% compared to its original value [15,16,19]. Most of the tests reported in the literature analyse the structural behaviour of masonry walls in case of fire. In contrast, the analysis of different structural elements (such as vaults and arches) is limited to only two cases described in [13,14]; it is, therefore, clear the need to fill this gap and carry out other experimental campaigns in order to characterise their behaviour when subjected to high temperatures. At the same time, the study of simple numerical models capable of describing the main phenomena occurring in masonry structures under fire conditions and their implementation in easy-to-use open-source numerical codes is paramount. From a numerical point of view, two different approaches can be used to investigate the behaviour of masonry structures under fire, i.e. limit analysis and finite element (FE) simulations. Relative to the first one, the only contribution present in the literature is [13], in which the Authors proposed a method to predict the loadbearing capacity of arches and vaults based on the simplified procedure described in the Eurocode 6 [7] typically used to assess the capacity of walls and columns. In detail, they applied the limit analysis method to reduced cross-sections of symmetrical curvilinear elements (in terms of geometry, material properties and load arrangement, with respect to the keystone cross-section) and validated the approach by exploiting the experimental test results carried out on two arches subjected to the standard fire load in the intrados and different distributed loads on the extrados. Regarding FE analysis, most of the papers in the literature deal with uncoupled thermomechanical analyses of walls or wall portions adopting a macro or micro modelling approach. In [20], a 3D micro-modelling approach has been employed to assess the spalling of two (load and non-load-bearing) masonry walls made of hollow bricks and traditional mortar during fire exposure. The simulation results, related to non-load-bearing walls carried out considering the nonlinear elastic behaviours of the materials, showed good agreement with the experimental tests performed. In contrast, as far as load-bearing walls are concerned, further investigations are needed. A micro model discretisation has also been used by [10] to simulate the residual behaviour of masonry prisms made of bricks and mortar exposed to elevated temperatures. The numerical investigations, performed using a quasi-brittle material constitutive law, seemed promising and were able to replicate the residual compressive strength of the masonry system. The Authors of [21,22] applied an uncoupled FE modelling approach to explore the residual mechanical performance of load-bearing masonry walls after insulation failure, focusing on the influence of wall thickness, masonry units and their void percentage. The simulations, run by DIANA software, consisted of a nonlinear transient heat flow stress analysis up to insulation failure, followed by a "cold" structural analysis in compression on the model after cooling. DIANA code has also been employed to develop a 2-D finite element based micro modelling framework for thermo-mechanical analysis of solid brick masonry structures subjected to fire, described in [23]. The framework considered geometric and material nonlinearities by total strain rotating crack model and transient states of strain with temperature-dependent material properties. The FE predictions were validated against the experimental response of a half-scale masonry wall subjected to one-sided fire exposure. In [24,25], the Authors describe a procedure to estimate the deformed configuration (bowing) of masonry walls exposed to fire, considering the geometrical and material characteristics of the blocks and joints through a homogenisation method. Compared to available experimental data, the results obtained show that the numerical model can roughly predict the deformation of walls even if limited to an elastic model for the constituent materials. Finally, [26] presents three modelling strategies to simulate the mechanical behaviour of the main structural elements of Notre-Dame de Paris Cathedral before and after the fire: two discrete block-to-block 3D approaches (DEM and FEM) and one continuum 3D approach (FEM). The results obtained proved the efficiency and robustness of the tools for establishing a comparative diagnosis of the stability of the structure, despite the simplified hypotheses on the thermomechanical behaviour of materials under the action of fire and its extinction.

An in-depth investigation on the numerical modelling of the static behaviour of masonry solids subjected to thermal loads was addressed in [27,28], where the constitutive equation of *masonry-like* materials [29,30] with zero tensile strength e infinite compressive strength is generalised to the non-isothermal case to consider thermal dilatations due to temperature variations. The equation has been implemented in NOSA-ITACA (www.nosaitaca.it/software/), a FE code, developed by ISTI-CNR, for the static [31] and dynamic structural analysis [32] of masonry constructions also in non-isothermal conditions [33]. The present work originates from the necessity to extend the constitutive equation of no-tension materials under non-isothermal conditions [30] to the case in which the masonry has weak tensile strength and bounded compressive strength, even temperature dependent. Furthermore, dealing with historical masonry structures means poor knowledge of the thermo-mechanical properties of the constituent materials, which generally cannot be improved by in situ tests. So, the paper shows how, through a simple constitutive model, whose application requires knowledge of a limited number of parameters, it is possible to assess the behaviour of historical masonry structures subjected to fire and estimate their bearing capacity in post-fire conditions. To this aim, in Section 2, the constitutive law for isotropic *masonry-like* materials is recalled and extended to the case of limited mechanical strength and non-isothermal conditions. In Section 3, the developed equation, implemented in NOSA-ITACA, is validated by using an artificial example. Finally, Section 4 shows its application to a masonry vault in fire conditions, tested by Vigili del Fuoco [14].

2. No tension materials with weak tensile strength and bounded compressive strength under non-isothermal conditions

In this section, the constitutive equation of the *masonry-like* materials under non-isothermal conditions [30] is recalled. The equation considers masonry as a homogeneous and isotropic nonlinear elastic material with zero or low tensile strength and infinite or limited compressive strength and can realistically model the most significant aspects of masonry's behaviour; here, the equation is generalised under the hypothesis of temperature-dependent tensile and compressive strength.

Denoting by Lin the space of the second-order tensors, let Sym be the subspace of all symmetric elements of Lin with the scalar product $\mathbf{A} \cdot \mathbf{B} = tr(\mathbf{AB})$ for any $\mathbf{A}, \mathbf{B} \in Sym$. Being Sym^- and Sym^+ the sets of all negative-semidefinite and positive-semidefinite

elements of Sym. Given the symmetric tensors $\mathbf{A}$ and $\mathbf{B}$, we denote by $\mathbf{A}\otimes\mathbf{B}$ the fourth-order tensor defined by $\mathbf{A}\otimes\mathbf{B}[\mathbf{H}] = (\mathbf{B}\cdot\mathbf{H})\mathbf{A}$ for $\mathbf{H}\in Lin$ and by $\mathbb{I}$ the fourth-order identity tensor on Sym.

Let $\vartheta\in[\vartheta_1,\vartheta_2]$, with $\vartheta_2>0$, be the absolute temperature and $\vartheta_0\in[\vartheta_1,\vartheta_2]$ the reference temperature. We assume that the thermal dilatation due to the temperature variation $(\vartheta-\vartheta_0)$ is the spherical tensor $\alpha(\vartheta-\vartheta_0)\mathbf{I}$ where α is the linear coefficient of thermal expansion and $\mathbf{I}$ the identity tensor.

Let $E(\vartheta)$, $\nu(\vartheta)$, $\sigma^t(\vartheta)$ and $\sigma^c(\vartheta)$ be the temperature-dependent elastic modulus, Poisson ratio, tensile and compressive strength respectively, and

$$\mu(\vartheta)=\frac{E(\vartheta)}{2(1+\nu(\vartheta))} \tag{1}$$

the temperature-dependent shear modulus.

Furthermore, let $\mathbb{C}(\vartheta)$ be the positive-definite, isotropic fourth-order elasticity tensor

$$\mathbb{C}(\vartheta)=\frac{E(\vartheta)}{1+\nu(\vartheta)}(\mathbb{I}+\frac{\nu(\vartheta)}{1-2\nu(\vartheta)}\mathbf{I}\otimes\mathbf{I}). \tag{2}$$

Let us set

$$\gamma(\vartheta)=\frac{\nu(\vartheta)}{1-2\nu(\vartheta)} \tag{3}$$

$$\beta(\vartheta)=\alpha(\vartheta-\vartheta_0), \tag{4}$$

and

$$\tilde{\omega}^t(\vartheta)=\frac{\sigma^t(\vartheta)}{2\mu(\vartheta)},\tilde{\omega}^c(\vartheta)=\frac{\sigma^c(\vartheta)}{2\mu(\vartheta)} \tag{5}$$

A masonry like material under non-isothermal conditions is an elastic material characterised by the fact that for $\mathbf{E}\in Sym$, and $\vartheta\in[\vartheta_1,\vartheta_2]$ there exists a unique quadruplet $(\mathbf{T},\mathbf{E}^e,\mathbf{E}^f,\mathbf{E}^c)$ of elements of Sym such that:

$$\begin{cases}\mathbf{T}-\sigma^t(\vartheta)\mathbf{I}\in Sym^-\\ \mathbf{T}+\sigma^c(\vartheta)\mathbf{I}\in Sym^+\\ \mathbf{E}-\beta(\vartheta)\mathbf{I}=\mathbf{E}^e+\mathbf{E}^f+\mathbf{E}^c\\ \mathbf{T}=\mathbb{C}(\vartheta)[\mathbf{E}^e]\\ \mathbf{E}^f\in Sym^+\\ \mathbf{E}^c\in Sym^-\\ \mathbf{E}^c\cdot\mathbf{E}^f=0\\ (\mathbf{T}-\sigma^t(\vartheta))\cdot\mathbf{E}^f=(\mathbf{T}+\sigma^c(\vartheta))\cdot\mathbf{E}^c=0\end{cases} \tag{6}$$

with $\mathbf{T}$ the Cauchy stress related to the infinitesimal strain $\mathbf{E}$. Tensors $\mathbf{E}^e$, $\mathbf{E}^f$ and $\mathbf{E}^c$ are the elastic, fracture and crushing parts of $\mathbf{E}$.

Since $\mathbb{C}$ is isotropic, it follows that tensors $\mathbf{E},\mathbf{E}^e,\mathbf{E}^f,\mathbf{E}^c,\mathbf{T},\mathbf{T}-\sigma^t(\vartheta),\mathbf{T}+\sigma^c(\vartheta)$ are coaxial [30], so the constitutive equation can be rewritten with respect to the basis $\{\mathbf{q_1},\mathbf{q_2},\mathbf{q_3}\}$ of the eigenvectors of $\mathbf{E}$. Let (e_1,e_2,e_3), (e_1^f,e_2^f,e_3^f), (e_1^c,e_2^c,e_3^c) and (t_1,t_2,t_3) be the eigenvalues of $\mathbf{E}$, $\mathbf{E}^f$, $\mathbf{E}^c$ and $\mathbf{T}$, respectively; it is easy to prove that (6) is equivalent to the system

$$\begin{cases}t_1=2\mu\{(e_1-\beta(\vartheta)-e_1^f-e_1^c)+\gamma[tr(\mathbf{E}-\beta(\vartheta)\mathbf{I})-tr(\mathbf{E}^f)-tr(\mathbf{E}^c)]\}\\ t_2=2\mu\{(e_2-\beta(\vartheta)-e_2^f-e_2^c)+\gamma[tr(\mathbf{E}-\beta(\vartheta)\mathbf{I})-tr(\mathbf{E}^f)-tr(\mathbf{E}^c)]\}\\ t_3=2\mu\{(e_3-\beta(\vartheta)-e_3^f-e_3^c)+\gamma[tr(\mathbf{E}-\beta(\vartheta)\mathbf{I})-tr(\mathbf{E}^f)-tr(\mathbf{E}^c)]\}\\ (t_1-\sigma^t(\vartheta))e_1^f=0\\ (t_2-\sigma^t(\vartheta))e_2^f=0\\ (t_3-\sigma^t(\vartheta))e_3^f=0\\ (t_1+\sigma^c(\vartheta))e_1^c=0\\ (t_2+\sigma^c(\vartheta))e_2^c=0\\ (t_3+\sigma^c(\vartheta))e_3^c=0\\ e_1^f\geq 0,e_2^f\geq 0,e_3^f\geq 0\\ e_1^c\leq 0,e_2^c\leq 0,e_3^c\leq 0\\ (t_1-\sigma^t(\vartheta))\leq 0,(t_2-\sigma^t(\vartheta))\leq 0,(t_3-\sigma^t(\vartheta))\leq 0\\ (t_1+\sigma^c(\vartheta))\geq 0,(t_2+\sigma^c(\vartheta))\geq 0,(t_3+\sigma^c(\vartheta))\geq 0\\ e_1^fe_1^c=0,e_2^fe_2^c=0,e_3^fe_3^c=0\end{cases} \tag{7}$$

where $tr(\mathbf{E}) = (e_1 + e_2 + e_3)$, $tr(\mathbf{E}^f) = (e_1^f + e_2^f + e_3^f)$ and $tr(\mathbf{E}^c) = (e_1^c + e_2^c + e_3^c)$. Given $E(\vartheta)$, $\nu(\vartheta)$, $\sigma^t(\vartheta)$ and $\sigma^c(\vartheta)$, it is possible to solve (7) and obtain the principal components of the stress, fracture and crushing tensors, defined in the following subsets, $\mathcal{R}_1$,..$\mathcal{R}_{10}$, of Sym.

If

$$\begin{aligned}&\mathbf{E} \in \mathcal{R}_1 = \{\mathbf{E} \in Sym \mid e_3 - \beta + \gamma[tr(\mathbf{E}) - 3\beta] - \tilde{\omega}^t \le 0,\\ &e_1 - \beta + \gamma[tr(\mathbf{E}) - 3\beta] + \tilde{\omega}^c \ge 0\},\end{aligned} \tag{8}$$

then

$$\begin{aligned}&e_1^f = e_2^f = e_3^f = 0,\\ &e_1^c = e_2^c = e_3^c = 0,\\ &t_1 = 2\mu[(1+\gamma)(e_1 - \beta) + \gamma(e_2 + e_3 - 2\beta)],\\ &t_2 = 2\mu[(1+\gamma)(e_2 - \beta) + \gamma(e_1 + e_3 - 2\beta)],\\ &t_3 = 2\mu[(1+\gamma)(e_3 - \beta) + \gamma(e_1 + e_2 - 2\beta)].\end{aligned} \tag{9}$$

Masonry is undamaged, with nil cracking and crushing strain, and exhibits linear elastic behaviour.

If

$$\begin{aligned}&\mathbf{E} \in \mathcal{R}_2 = \{\mathbf{E} \in Sym \mid e_1 - \beta + \gamma[tr(\mathbf{E}) - 3\beta] + \tilde{\omega}^c < 0,\\ &\gamma(e_2 - \beta) + (1+\gamma)(e_3 - \beta) - \gamma\tilde{\omega}^c - (1+\gamma)\tilde{\omega}^t < 0,\\ &(1+2\gamma)(e_2 - \beta) + \gamma(e_3 - \beta) + \tilde{\omega}^c \ge 0\},\end{aligned} \tag{10}$$

then

$$\begin{aligned}&e_1^f = e_2^f = e_3^f = 0,\\ &e_1^c = (e_1 - \beta) + \frac{\gamma}{1+\gamma}(e_2 + e_3 - 2\beta) + \frac{\tilde{\omega}^c}{1+\gamma},\\ &e_2^c = e_3^c = 0,\\ &t_1 = -\sigma^c,\\ &t_2 = 2\mu[(e_2 - \beta) + \frac{\gamma}{1+\gamma}(e_2 + e_3 - 2\beta - \tilde{\omega}^c)],\\ &t_3 = 2\mu[(e_3 - \beta) + \frac{\gamma}{1+\gamma}(e_2 + e_3 - 2\beta - \tilde{\omega}^c)].\end{aligned} \tag{11}$$

Masonry achieves the compressive strength along a principal direction, resulting in crushing strain; no cracking strain develops, and the material exhibits linear elastic behaviour under tensile stresses.

If

$$\begin{aligned}&\mathbf{E} \in \mathcal{R}_3 = \{\mathbf{E} \in Sym \mid (1+2\gamma)(e_2 - \beta) + \gamma(e_3 - \beta) + \tilde{\omega}^c < 0,\\ &(1+3\gamma)(e_3 - \beta) - 2\gamma\tilde{\omega}^c - (1+\gamma)\tilde{\omega}^t < 0,\\ &(1+3\gamma)(e_3 - \beta) + \tilde{\omega}^c \ge 0\},\end{aligned} \tag{12}$$

then

$$\begin{aligned}&e_1^f = e_2^f = e_3^f = 0,\\ &e_1^c = (e_1 - \beta) + \frac{\gamma}{(1+2\gamma)}(e_3 - \beta) + \frac{\tilde{\omega}^c}{(1+2\gamma)},\\ &e_2^c = (e_2 - \beta) + \frac{\gamma}{(1+2\gamma)}(e_3 - \beta) + \frac{\tilde{\omega}^c}{(1+2\gamma)},\\ &e_3^c = 0,\\ &t_1 = -\sigma^c,\\ &t_2 = -\sigma^c,\\ &t_3 = \frac{2\mu}{1+2\gamma}[(1+3\gamma)(e_3 - \beta) - 2\gamma\tilde{\omega}^c]\}.\end{aligned} \tag{13}$$

Masonry crushes along two principal directions, while no fracture strain occurs; this implies that any tensile stress is lower than the material's tensile strength.

If

$$\mathbf{E} \in \mathcal{R}_4 = \{\mathbf{E} \in Sym \mid (1+3\gamma)(e_3 - \beta) + \tilde{\omega}^c < 0\} \tag{14}$$

then

$$\begin{aligned} &e_1^f = e_2^f = e_3^f = 0, \\ &e_1^c = (e_1 - \beta) + \frac{\tilde{\omega}^c}{1+3\gamma} \\ &e_2^c = (e_2 - \beta) + \frac{\tilde{\omega}^c}{1+3\gamma} \\ &e_3^c = (e_3 - \beta) + \frac{\tilde{\omega}^c}{1+3\gamma} \\ &t_1 = t_2 = t_3 = -\sigma^c. \end{aligned} \tag{15}$$

Masonry is completely crushed having reached its maximum compressive strength; crushing strains arise along the three principal directions.

If

$$\begin{aligned} &\mathbf{E} \in \mathcal{R}_5 = \{\mathbf{E} \in Sym \mid (e_3 - \beta) + \gamma[tr(\mathbf{E}) - 3\beta] - \tilde{\omega}^t > 0, \\ &(1+2\gamma)(e_2 - \beta) + \gamma(e_1 - \beta) - \tilde{\omega}^t \leq 0, \\ &(1+\gamma)(e_1 - \beta) + \gamma(e_2 - \beta) + 2\gamma\tilde{\omega}^t + (1+\gamma)\tilde{\omega}^c > 0\}, \end{aligned} \tag{16}$$

then

$$\begin{aligned} &e_1^f = e_2^f = 0, \\ &e_3^f = (e_3 - \beta) + \frac{\gamma}{1+\gamma}(e_1 + e_2 - 2\beta) - \frac{\tilde{\omega}^t}{1+\gamma}, \\ &e_1^c = e_2^c = e_3^c = 0, \\ &t_1 = \frac{2\mu}{1+\gamma}[(1+2\gamma)(e_1 - \beta) + \gamma(e_2 - \beta) + \gamma\tilde{\omega}^t], \\ &t_2 = \frac{2\mu}{1+\gamma}[(1+2\gamma)(e_2 - \beta) + \gamma(e_1 - \beta) + \gamma\tilde{\omega}^t], \\ &t_3 = \sigma^t. \end{aligned} \tag{17}$$

Masonry is cracked along one principal direction (where one of the stress tensor eigenvalues is equal to the material's tensile strength), while under compression, masonry can exhibits linear elastic behaviour.

If

$$\begin{aligned} &\mathbf{E} \in \mathcal{R}_6 = \{\mathbf{E} \in Sym \mid (1+2\gamma)(e_2 - \beta) + \gamma(e_1 - \beta) - \tilde{\omega}^t > 0, \\ &(1+3\gamma)(e_1 - \beta) - \tilde{\omega}^t \leq 0, \\ &(1+3\gamma)(e_1 - \beta) + 2\gamma\tilde{\omega}^t + (1+2\gamma)\tilde{\omega}^c \geq 0\}, \end{aligned} \tag{18}$$

then

$$\begin{aligned} &e_1^f = 0, \\ &e_2^f = (e_2 - \beta) + \frac{\gamma}{(1+2\gamma)}(e_1 - \beta) - \frac{\tilde{\omega}^t}{(1+2\gamma)}, \\ &e_3^f = (e_3 - \beta) + \frac{\gamma}{(1+2\gamma)}(e_1 - \beta) - \frac{\tilde{\omega}^t}{(1+2\gamma)}, \\ &e_1^c = e_2^c = e_3^c = 0, \\ &t_1 = \frac{2\mu}{1+2\gamma}[(1+3\gamma)(e_1 - \beta) + 2\gamma\tilde{\omega}^t], \\ &t_2 = t_3 = \sigma^t; \end{aligned} \tag{19}$$

Masonry reaches the maximum tensile strength along two principal directions (with the corresponding cracks formation).

If

$$\mathbf{E} \in \mathcal{R}_7 = \{\mathbf{E} \in Sym \mid (1+3\gamma)(e_1 - \beta) - \tilde{\omega}^t > 0\} \tag{20}$$

then

$$\begin{aligned} &e_1^f = (e_1 - \beta) - \frac{\tilde{\omega}^t}{1+3\gamma}, \\ &e_2^f = (e_2 - \beta) - \frac{\tilde{\omega}^t}{1+3\gamma}, \\ &e_3^f = (e_3 - \beta) - \frac{\tilde{\omega}^t}{1+3\gamma}, \\ &e_1^c = e_2^c = e_3^c = 0, \\ &t_1 = t_2 = t_3 = \sigma^t. \end{aligned} \tag{21}$$

Masonry is unable to withstand tensile stresses greater than its tensile strength; cracking strains, different from zero, arise along the principal directions.

If

$$\begin{aligned}&\mathbf{E} \in \mathcal{R}_8 = \{\mathbf{E} \in Sym \mid (1+3\gamma)(e_2-\beta) - \gamma\tilde{\omega}^c - (1+\gamma)\tilde{\omega}^t \geq 0,\\ &(1+3\gamma)(e_1-\beta) + 2\gamma\tilde{\omega}^t + (1+2\gamma)\tilde{\omega}^c < 0\}\end{aligned} \tag{22}$$

then

$$\begin{aligned}&e_1^f = 0,\\ &e_2^f = (e_2-\beta) - \frac{\gamma\tilde{\omega}^c}{(1+3\gamma)} - \frac{1+\gamma}{(1+3\gamma)}\tilde{\omega}^t,\\ &e_3^f = (e_3-\beta) - \frac{\gamma\tilde{\omega}^c}{(1+3\gamma)} - \frac{2+\gamma}{(1+3\gamma)}\tilde{\omega}^t,\\ &e_1^c = (e_1-\beta) + \frac{(1+2\gamma)\tilde{\omega}^c}{1+3\gamma} + \frac{2\gamma}{1+3\gamma}\tilde{\omega}^t,\\ &e_2^c = e_3^c = 0,\\ &t_1 = -\sigma^c,\\ &t_2 = t_3 = \sigma^t.\end{aligned} \tag{23}$$

Masonry is cracked along two principal directions and crushed along one; its tensile and compressive strength are reached along all the principal directions.

If

$$\begin{aligned}&\mathbf{E} \in \mathcal{R}_9 = \{\mathbf{E} \in Sym \mid (1+3\gamma)(e_2-\beta) + \gamma\tilde{\omega}^t + (1+\gamma)\tilde{\omega}^c \leq 0,\\ &(1+3\gamma)(e_3-\beta) - 2\gamma\tilde{\omega}^c - (1+\gamma)\tilde{\omega}^t > 0\},\end{aligned} \tag{24}$$

then

$$\begin{aligned}&e_1^f = e_2^f = 0,\\ &e_3^f = (e_3-\beta) - \frac{2\gamma\tilde{\omega}^c}{1+3\gamma} - \frac{1+2\gamma}{1+3\gamma}\tilde{\omega}^t,\\ &e_1^c = (e_1-\beta) + \frac{(1+\gamma)\tilde{\omega}^c}{(1+3\gamma)} + \frac{\gamma}{(1+3\gamma)}\tilde{\omega}^t,\\ &e_2^c = (e_2-\beta) + \frac{(1+\gamma)\tilde{\omega}^c}{(1+3\gamma)} + \frac{\gamma}{(1+3\gamma)}\tilde{\omega}^t,\\ &e_3^c = 0,\\ &t_1 = t_2 = -\sigma^c,\\ &t_3 = \sigma^t.\end{aligned} \tag{25}$$

Masonry crushed along two principal directions and cracked along one; the eigenvalues of the stress tensor are equal to the compressive and tensile strength.

Finally, if

$$\begin{aligned}&\mathbf{E} \in \mathcal{R}_{10} = \{\mathbf{E} \in Sym \mid (1+2\gamma)(e_1-\beta) + \gamma(e_2-\beta) + \gamma\tilde{\omega}^t + (1+\gamma)\tilde{\omega}^c < 0,\\ &(1+2\gamma)(e_3-\beta) + \gamma(e_2-\beta) - \gamma\tilde{\omega}^c - (1+\gamma)\tilde{\omega}^t > 0,\\ &(1+3\gamma)(e_2-\beta) - \gamma\tilde{\omega}^c - (1+\gamma)\tilde{\omega}^t < 0,\\ &(1+3\gamma)(e_2-\beta) + \gamma\tilde{\omega}^t + (1+\gamma)\tilde{\omega}^c > 0\},\end{aligned} \tag{26}$$

$$\begin{aligned}&e_1^f = e_2^f = 0,\\ &e_3^f = (e_3-\beta) + \frac{\gamma}{(1+2\gamma)}(e_2-\beta) - \frac{1+\gamma}{(1+2\gamma)}\tilde{\omega}^t - \frac{\gamma}{(1+2\gamma)}\tilde{\omega}^c,\\ &e_1^c = (e_1-\beta) + \frac{\gamma}{(1+2\gamma)}(e_2-\beta) + \frac{1+\gamma}{(1+2\gamma)}\tilde{\omega}^c + \frac{\gamma}{(1+2\gamma)}\tilde{\omega}^t,\\ &e_2^c = e_3^c = 0,\\ &t_1 = -\sigma^c,\\ &t_2 = \frac{2\mu}{(1+2\gamma)}[(1+3\gamma)(e_2-\beta) + \gamma(\tilde{\omega}^t - \tilde{\omega}^c)],\\ &t_3 = \sigma^t;\end{aligned} \tag{27}$$

Masonry reaches its maximum tensile and compressive strength along two principal directions; the material exhibits cracking and crushing strain different from zero. Meanwhile, along the second direction, it shows linear elastic behaviour.

It is easy to prove that in regions $\mathcal{R}_2$, $\mathcal{R}_6$ and $\mathcal{R}_8$ $e_1 < e_2 \leq e_3$ and that in $\mathcal{R}_3$, $\mathcal{R}_5$ and $\mathcal{R}_9$, $e_1 \leq e_2 < e_3$. Lastly, the eigenvalues of $\mathbf{E}$ are distinct in $\mathcal{R}_{10}$. The explicit expression of the derivatives of the stress function with respect to the strain tensor can be

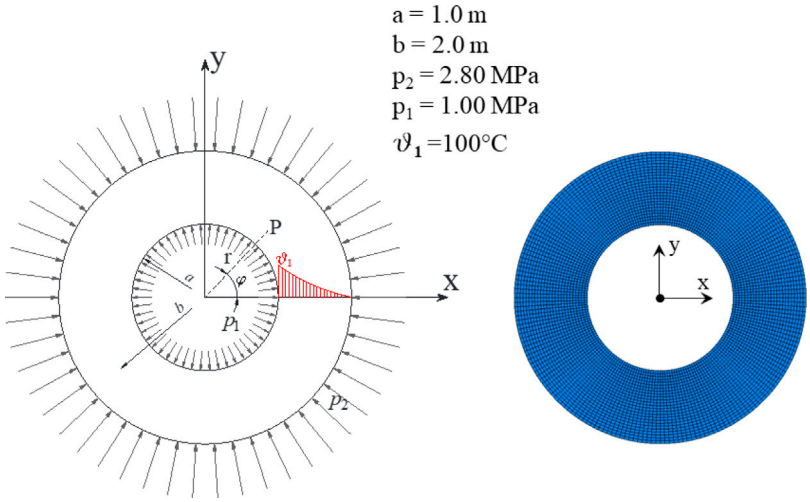

Fig. 1. The circular ring (left) and its mesh (right) created by NOSA-ITACA.

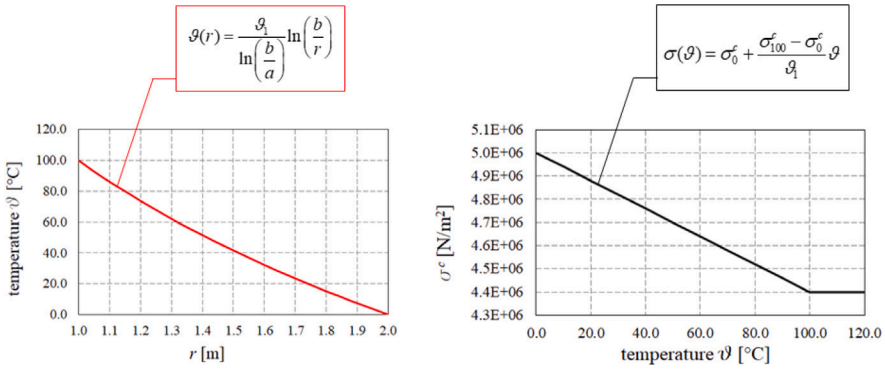

Fig. 2. Stationary temperature field in the ring (left) and temperature versus compressive strength (right).

calculated in the same way shown in [30]. These derivatives are then used to calculate, for each strain tensor **E**, the tangent stiffness matrix employed in the numerical procedure implemented in NOSA-ITACA to solve the equilibrium problem and based on the Newton–Raphson iterative scheme; for sake of brevity this part is omitted [30].

3. Numerical examples

In this section, two different examples are examinated, with the aim of validating the constitute law described in Section 2 and its implementation in the finite element code NOSA-ITACA. In the first example, a circular ring (Fig. 1) subjected to a plane strain condition, resulting from uniform radial pressures p_2 and p_1 and a stationary temperature field due to a steady heat flow (cf. relation (28), Fig. 2) is considered modelling the constituent material as a masonry-like material with zero tensile strength and temperature independent compressive strength. The explicit solution of the problem is determined and compared with the numerical one calculated by NOSA-ITACA in terms of stress components, crushing strain and displacement. The second example follows the previous one, but the analysis is conducted under the hypothesis that the compressive strength depends linearly on temperature (cf. relation (46), Fig. 2). Also in this case the analytic solution is compared with the one obtained from the FE code.

3.1. The circular ring made of masonry-like material with temperature independent compressive strength.

The circular ring, sketched in Fig. 1, with a inner radius a and outer radius b, is subjected to two uniform radial pressures p_2 and p_1, acting uniformly on the outer and inner surface, and a steady temperature field varying with radius r:

$$\vartheta(r) = \frac{\vartheta_1}{\log(\frac{b}{a})} \log(\frac{b}{r}) \tag{28}$$

with $\vartheta_1 > 0$ the absolute value of the temperature on the inner surface. In the following let it be E the Young's modulus, ν the Poisson's ratio, $\vartheta_0 = 0$ the reference temperature and $\beta = \alpha\vartheta$ the thermal expansion with constant α. A polar reference system $\{O, \mathrm{r}, \varphi\}$, whose origin coincides with the centre of the ring and the z-axis orthogonal to its plane, is chosen to analyse the problem; because of symmetry, the only non-zero displacement is the radial component $u(r)$.

The solution to the equilibrium problem of a circular ring made of a homogeneous isotropic linear elastic material subjected to pressure p_1 and p_2 and having the temperature distribution (28) can be expressed as the sum of the solutions of two problems [34]:

$$\begin{aligned} \sigma_r(r) &= \sigma_r^p(r) + \sigma_r^t(r), \\ \sigma_\varphi(r) &= \sigma_\varphi^p(r) + \sigma_\varphi^t(r), \end{aligned} \tag{29}$$

with $\sigma_r(r)$ and $\sigma_\varphi(r)$ the radial and circumferential component of the stress tensor;

$$\begin{aligned} \sigma_r^p(r) &= \frac{1}{b^2 - a^2}[p_1 a^2 - p_2 b^2 + a^2 b^2 (p_2 - p_1)\frac{1}{r^2}], \\ \sigma_\varphi^p(r) &= \frac{1}{b^2 - a^2}[p_1 a^2 - p_2 b^2 - a^2 b^2 (p_2 - p_1)\frac{1}{r^2}], \end{aligned} \tag{30}$$

the stress field in the circular ring due to the outer and inner pressure surface and

$$\begin{aligned} \sigma_r^t(r) &= k[-\log(\frac{b}{r}) - \frac{a^2}{b^2 - a^2}(1 - \frac{b^2}{r^2})\log(\frac{b}{a})] \\ \sigma_\varphi^t(r) &= k[1 - \log(\frac{b}{r}) - \frac{a^2}{b^2 - a^2}(1 + \frac{b^2}{r^2})\log(\frac{b}{a})] \\ k &= \frac{\alpha E \vartheta_1}{2(1-\nu)\log(\frac{b}{a})} \end{aligned} \tag{31}$$

the resulting stress field of the stationary temperature load.

Let us assume that p_1 and p_2 verify the condition:

$$\frac{a^2 + b^2}{2b^2} p_1 \leq p_2 \leq \frac{a^2 + b^2}{2b^2} p_1 + \frac{b^2 - a^2}{2b^2}\sigma^c, \tag{32}$$

Then, $\sigma_\varphi^p(r)$ and $\sigma_r^p(r)$ are monotonic functions of r and not positive [30]. If $\vartheta_1 > 0$, $\sigma_r^t(r)$ is negative at every point and nil on the edge and $\sigma_\varphi^t(r)$ is negative for $r = a$ [34]. The condition for which $\sigma_\varphi(b) \leq 0$ implies that:

$$\alpha\vartheta_1 \leq \frac{2(1-\nu)}{E}\frac{p_2(1+\eta^2) - 2p_1}{\eta^2 - 2\log\eta - 1} log\eta, \tag{33}$$

where we set

$$\eta = \frac{b}{a}. \tag{34}$$

Following an approach similar to that used in [35] is possible to prove that the circumferential stress is still non-positive for each $r \in [a, b]$; the proof of this statement is omitted for sake of brevity.

Let us now assume the circular ring made of a *masonry-like* material with zero tensile strength and limited compressive strength σ^c not depending on temperature. In seeking the solution, and by virtue of (32), tentatively suppose that the strain belongs to the region in $\mathcal{R}_2$ (10) assuming the circumferential stress $\sigma_\varphi(r) = t_1 = -\sigma^c$ (11) in a portion of the circular ring $\Omega_1 = \{(r, \varphi) : r \in [a, r_c]\}$, where the radius r_c is unknown. In this region, from the equilibrium equation:

$$\frac{d\sigma_r}{dr} + \frac{\sigma_r - \sigma_\varphi}{r} = 0 \tag{35}$$

By virtue of (11), we get

$$\sigma_r = \frac{E}{1-\nu^2}[\varepsilon_r - \alpha\vartheta(1+\nu)] - \frac{\nu}{1-\nu}\sigma^c, \tag{36}$$

where $\varepsilon_r = e_2$ is the radial strain, equal to the derivative with respect to the radius of the displacement $u(r)$:

$$\sigma_r = \frac{E}{1-\nu^2}[\frac{du}{dr} - \alpha\vartheta(1+\nu)] - \frac{\nu}{1-\nu}\sigma^c, \tag{37}$$

$$\frac{d\sigma_r}{dr} = \frac{E}{1-\nu^2}[\frac{d^2u}{dr^2} - \alpha(1+\nu)\frac{d\vartheta}{dr}] \tag{38}$$

The relation (35) is then equivalent to the differential equation

$$r\frac{d^2u}{dr^2} - \alpha r(1+\nu)\frac{d\vartheta}{dr} + \frac{du}{dr} - \alpha\vartheta(1+\nu) + \frac{\nu}{\lambda}\sigma^c = 0 \tag{39}$$

with $\lambda = \frac{E\nu}{(1+\nu)(1-2\nu)}$ the Lame constant. From (39) it follows

$$\frac{du}{dr} = \alpha\vartheta(1+\nu) + \frac{c}{r} - \frac{\nu}{\lambda}\sigma^c \tag{40}$$

which replaced in (37) gives

$$\sigma_r(r) = \frac{E}{1-\nu^2}\frac{c}{r} - \sigma^c \tag{41}$$

The constant c can be determined imposing the boundary condition $\sigma_r(a) = -p_1$ holding that $c = \frac{1-\nu^2}{E}a(\sigma^c - p_1)$.

In the remain circular ring $\Omega_2 = \{(r,\varphi) : r \in [r_c, b]\}$ the stress field will coincide with the linear elastic solution of a ring subjected to an external pressure p_2, an internal pressure $p_c = \sigma^c - \frac{a}{r_c}(\sigma^c - p_1)$ and the temperature distribution $\vartheta(r) = \frac{\vartheta_r}{\log(\frac{b}{r_c})}\log(\frac{b}{r})$ with $\vartheta_r = \frac{\vartheta_1}{\log(\frac{b}{a})}\log(\frac{b}{r_c})$ given from (28) assuming $r = r_c$.

The value of r_c that separates Ω_1 and Ω_2 can be estimated imposing the continuity of $\sigma_\varphi(r)$ at $r = r_c$:

$$\begin{aligned} -\sigma^c &= \sigma_\varphi(r_c^-) = \sigma_\varphi(r_c^+) \\ \sigma_\varphi(r_c^+) &= \frac{p_c(b^2+r_c^2) - 2p_2b^2}{b^2 - r_c^2} + k[1 - \log(\frac{b}{r_c}) - \frac{r_c^2}{b^2-r_c^2}(1+\frac{b^2}{r_c^2})\log(\frac{b}{r_c})] \end{aligned} \tag{42}$$

Therefore, the solution in term of stress components is

$$\sigma_r(r) = \begin{cases} \frac{a}{r}(\sigma^c - p_1) - \sigma^c, & r \in [a, r_c] \\ \frac{r^2(p_c r_c^2 - p_2 b^2) + r_c^2 b^2 (p_2 - p_c)}{r^2(b^2 - r_c^2)} + k[-\log(\frac{b}{r}) - \frac{r_c^2}{b^2-r_c^2}(1-\frac{b^2}{r^2})\log(\frac{b}{r_c})], & r \in [r_c, b] \end{cases}$$

$$\sigma_\varphi(r) = \begin{cases} -\sigma^c, & r \in [a, \rho_c] \\ \frac{r^2(p_c r_c^2 - p_2 b^2) - r_c^2 b^2 (p_2 - p_c)}{r^2(b^2 - r_c^2)} + k[1 - \log(\frac{b}{r}) - \frac{r_c^2}{b^2-r_c^2}(1+\frac{b^2}{r^2})\log(\frac{b}{r_c})], & r \in [\rho_c, b] \end{cases}$$

From (40) and in virtue of (28) is possible to calculate the displacement u in Ω_1:

$$u = \alpha(1+\nu)\frac{\vartheta_1}{\log(\frac{b}{a})}[r\log(\frac{b}{r}) + r] + \frac{1-\nu^2}{E}a(\sigma^c - p_1)\log(r) - \frac{\nu}{\lambda}\sigma^c r + d \tag{43}$$

with d a constant which can be determined by imposing the continuity of $u(r)$ at $r = r_c$.

The displacement in Ω_2 it is:

$$u(r) = \frac{1-\nu^2}{E}r[\sigma_\varphi(r) - \frac{\nu}{1-\nu}\sigma_r(r)] + (1+\nu)\alpha\frac{\vartheta_r}{log\frac{b}{r_c}}rlog\frac{b}{r} \tag{44}$$

Finally, by virtue of (11), (40) and remembering that $e_1 = \varepsilon_\varphi = u(r)/r$ and $\varepsilon_r = \frac{du}{dr}$, it follows:

$$\varepsilon_\varphi^c(r) = \begin{cases} (\varepsilon_\varphi(r) - \alpha\vartheta) + \frac{\nu}{1-\nu}(\varepsilon_r(r) - 2\alpha\vartheta + \frac{\sigma^c}{\lambda}), & r \in [a, r_c] \\ 0, & r \in [r_c, b] \end{cases}$$

For the numerical calculation of the solution, the following values of the constants are used:

$$\begin{aligned} &a = 1.0\ \text{m}, b = 2.0\ \text{m} \\ &p_1 = 1.0\times10^6\ \text{Pa}, p_2 = 2.8\times10^6\ \text{Pa} \\ &\nu = 0.2, E = 3.0\times10^9\ \text{Pa}, \sigma^c = 5.0\times10^6\ \text{Pa} \\ &\alpha = 1\times10^{-5}(^\circ\text{C})^{-1} \\ &\vartheta_0 = 0\ ^\circ\text{C}, \vartheta_1 = 100\ ^\circ\text{C} \end{aligned} \tag{45}$$

With the aim of comparing the explicit solution with the numerical one calculated by means of the finite element code NOSA-ITACA, the ring is discretised into 20,000 4-node isoparametric quadrilateral elements with linear shape functions (corresponding to element 6 of NOSA-ITACA library) for a total of 20,200 nodes and 40,400 degrees of freedom (Fig. 1).

Fig. 3 shows the radial (top) and tangent (bottom) stresses for the circular ring obtained from the explicit solution (continuous red line) compared with the numerical solution achieved by the FE code (black bold points); as it is possible to note there is a perfect coincidence between the two results. In order to underline the different behaviours of a linear elastic material and a *masonry-like* material, the solution to the linear elastic problem is also depicted in the Figure by a dotted red line. The radial displacement (top) and the crushing strain component (bottom) calculated analytically (continuous red line) and numerically (black bold points) are compared in Fig. 4. Again, the two solutions coincide, even in terms of the radius of transition value $r_c = 1.56$m; furthermore, it is noted that the no-tension model leads to an increase in radial displacement of approximately 40%.

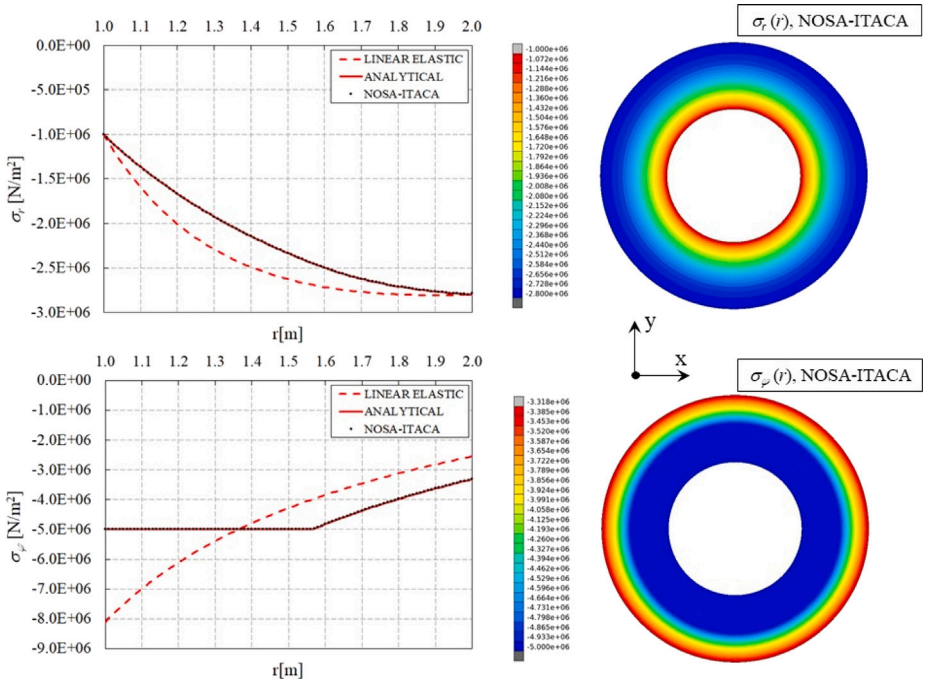

Fig. 3. Radial (top) and circumferential (bottom) stress component.

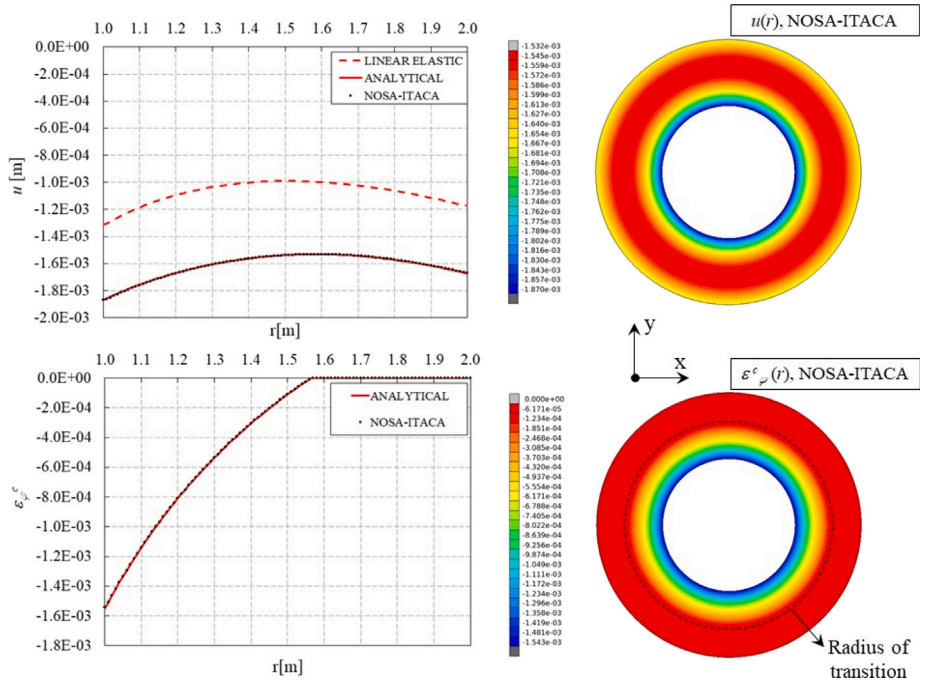

Fig. 4. Radial displacement (up) and circumferential (bottom) crushing strain.

3.2. The circular ring modelled by masonry-like material with temperature dependent compressive strength.

In the case of $\sigma^c = \sigma^c(\vartheta)$ and $\vartheta = \vartheta(r)$ expressed by (46) and (28) respectively, following a procedure similar to that used in Section 3.1 the equilibrium in radial direction (35), supposing to be again in region $\mathcal{R}_2$ (10), becomes:

$$\sigma^c(\vartheta) = \sigma_0^c + \frac{\sigma_{100}^c - \sigma_0^c}{\vartheta_1}\vartheta \tag{46}$$

$$r\frac{d^2u}{dr^2} + \frac{du}{dr} + k_1 + k_2 \log\frac{b}{r} = 0 \tag{47}$$

with k_1 and k_2 constant values equals to:

$$\begin{aligned} k_1 &= \frac{\vartheta_1}{log\frac{b}{a}}[\alpha(1+\nu) + \frac{\nu}{2\mu}\frac{\sigma_{100}^c - \sigma_0^c}{\vartheta_1}] + \frac{\nu}{\lambda}\sigma_0^c \\ k_2 &= \frac{\vartheta_1}{log\frac{b}{a}}[\frac{\sigma_{100}^c - \sigma_0^c}{\vartheta_1}\frac{\nu}{\lambda} - \alpha(1+\nu)] \end{aligned} \tag{48}$$

with σ_0^c and σ_{100}^c the compressive strength at $\vartheta_0 = 0$ °C and $\vartheta_{100} = 100$ °C, resp.

The solution of (47) can be expressed in the following form:

$$\frac{du}{dr} = \frac{c}{r} - k_1 - k_2(\log\frac{b}{r} + 1) \tag{49}$$

where the constant c is determined imposing the boundary condition $\sigma_r(a) = -p_1$:

$$c = a[\frac{1-\nu^2}{E}(\frac{\nu}{1-\nu}\sigma_{100}^c - p_1) + k_1 + k_2(1 + \log(\frac{b}{a})) + \alpha(1+\nu)\vartheta_1] \tag{50}$$

Again, it is possible to find the transition radius value r_c that separates the crushing zone from the linear elastic one, imposing the continuity of $\sigma_\varphi(r)$ at $r = r_c$. It follows:

$$\sigma_r(r) = \begin{cases} \frac{E}{1-\nu^2}[\frac{c}{r} - k_1 - k_2(1+\log(\frac{b}{r})) - \alpha q_1(1+\nu)\log(\frac{b}{r})] - \frac{\nu}{1-\nu}(\sigma_0^c + q_1 q\log(\frac{b}{r})), & r \in [a, r_c] \\ \frac{r^2(p_c r_c^2 - p_2 b^2) + r_c^2 b^2(p_2 - p_c)}{r^2(b^2 - r_c^2)} + k[-\log(\frac{b}{r}) - \frac{r_c^2}{b^2 - r_c^2}(1 - \frac{b^2}{r^2})\log(\frac{b}{r_c})], & r \in [r_c, b] \end{cases}$$

$$\sigma_\varphi(r) = \begin{cases} -\sigma_0^c - q_1 q\log(\frac{b}{r}), & r \in [a, \rho_c] \\ \frac{r^2(p_c r_c^2 - p_2 b^2) - r_c^2 b^2(p_2 - p_c)}{r^2(b^2 - r_c^2)} + k[1 - \log(\frac{b}{r}) - \frac{r_c^2}{b^2 - r_c^2}(1 + \frac{b^2}{r^2})\log(\frac{b}{r_c})], & r \in [\rho_c, b] \end{cases}$$

where:

$$\begin{aligned} q &= \frac{\sigma_{100}^c - \sigma_0^c}{\vartheta_1} \\ q_1 &= \frac{\vartheta_1}{log\frac{b}{a}} \\ p_c &= \frac{E}{1-\nu^2}[\frac{c}{r_c} - k_1 - k_2(1 + \log(\frac{b}{r_c})) - \alpha q_1(1+\nu)\log(\frac{b}{r_c})] - \frac{\nu}{1-\nu}(\sigma_0^c + q_1 q\log(\frac{b}{r_c})) \end{aligned} \tag{51}$$

The expression of radial displacement and circumferential crushing strain can be calculated as in the previous section and here, the step by step solution, is omitted for sake of brevity.

$$u(r) = \begin{cases} -k_2 r\log(\frac{b}{r}) + c log(r) - r(k_1 + 2k_2) + d, & r \in [a, r_c] \\ \frac{1-\nu^2}{E}r[\sigma_\varphi(r) - \frac{\nu}{1-\nu}\sigma_r(r)] + (1+\nu)\alpha\frac{\vartheta_r}{log\frac{b}{r_c}}r log\frac{b}{r}, & r \in [r_c, b] \end{cases}$$

$$\varepsilon_\varphi^c(r) = \begin{cases} (\varepsilon_\varphi(r) - \alpha\vartheta) + \frac{\nu}{1-\nu}(\varepsilon_r(r) - 2\alpha\vartheta + \frac{\sigma^c(r)}{\lambda}), & r \in [a, r_c] \\ 0, & r \in [r_c, b] \end{cases}$$

For the numerical solution, the following values are used:

$$\begin{aligned} &a = 1.0 \text{ m}, b = 2.0 \text{ m} \\ &p_1 = 1.0 \times 10^6 \text{ Pa}, p_2 = 2.8 \times 10^6 \text{ Pa} \\ &\nu = 0.2, E = 3.0 \times 10^9 \text{ Pa} \\ &\sigma_0^c = 5.00 \times 10^6 \text{ Pa}, \sigma_{100}^c = 4.25 \times 10^6 \text{ Pa} \\ &\alpha = 1 \times 10^{-5}(°\text{C})^{-1} \\ &\vartheta_0 = 0 \text{ °C}, \vartheta_1 = 100 \text{ °C} \end{aligned} \tag{52}$$

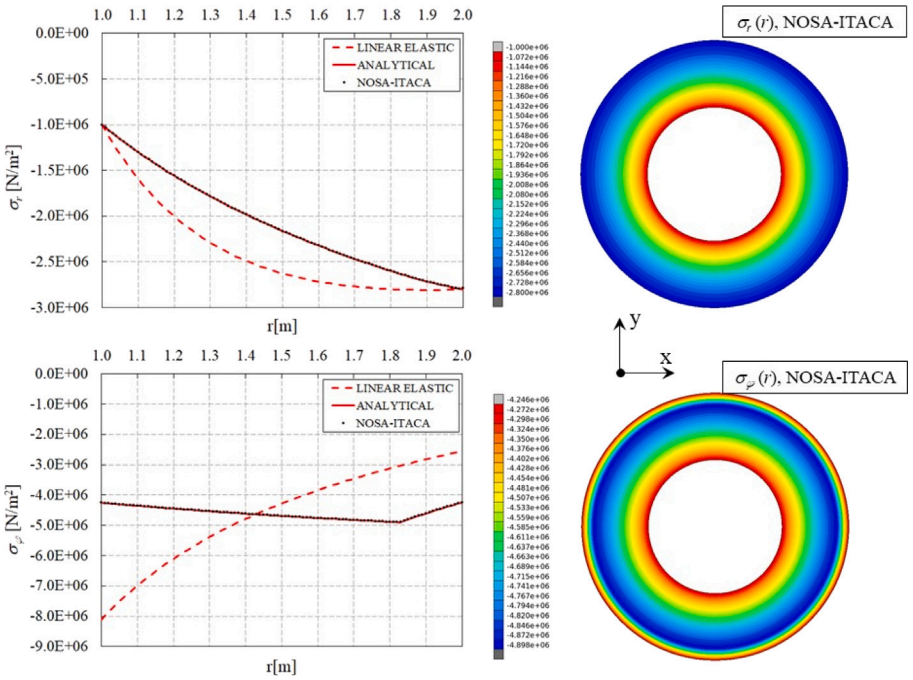

Fig. 5. Radial (top) and circumferential (bottom) stress component.

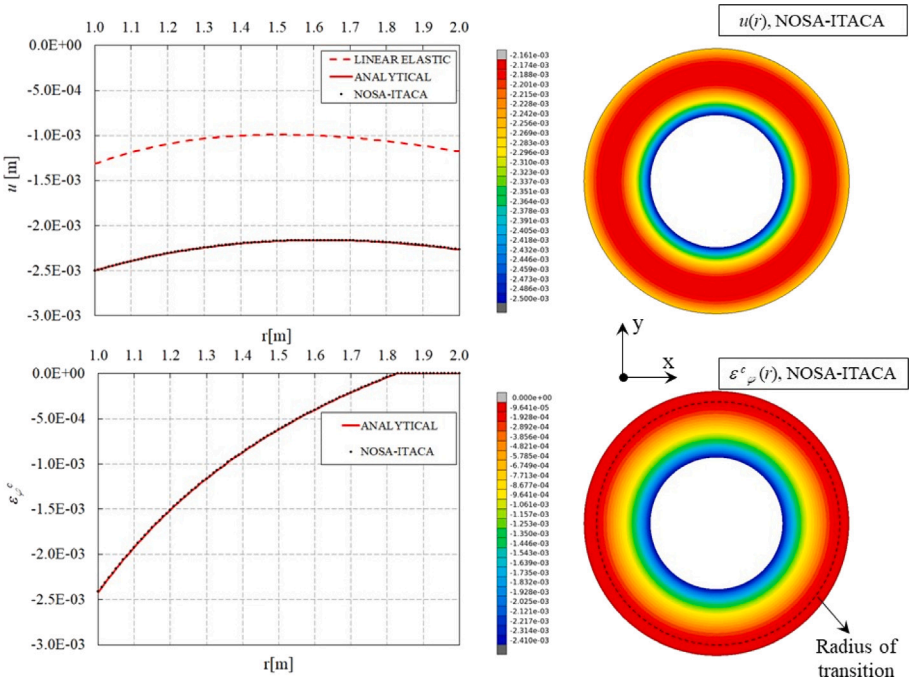

Fig. 6. Radial displacement (top) and circumferential (bottom) crushing strain.

In order to compare the numerical solution with the analytical one, the ring is still discretised into 20,000 4-node isoparametric quadrilateral elements with linear shape functions (corresponding to element 6 of NOSA-ITACA library) for a total of 20,200 nodes and 40,400 degrees of freedom.

Fig. 5 shows the radial (top) and tangent (bottom) stresses for the circular ring obtained from the explicit solution (continuous red line), and by the FE code (black bold points); again, it is possible to note a perfect coincidence between the two results. The

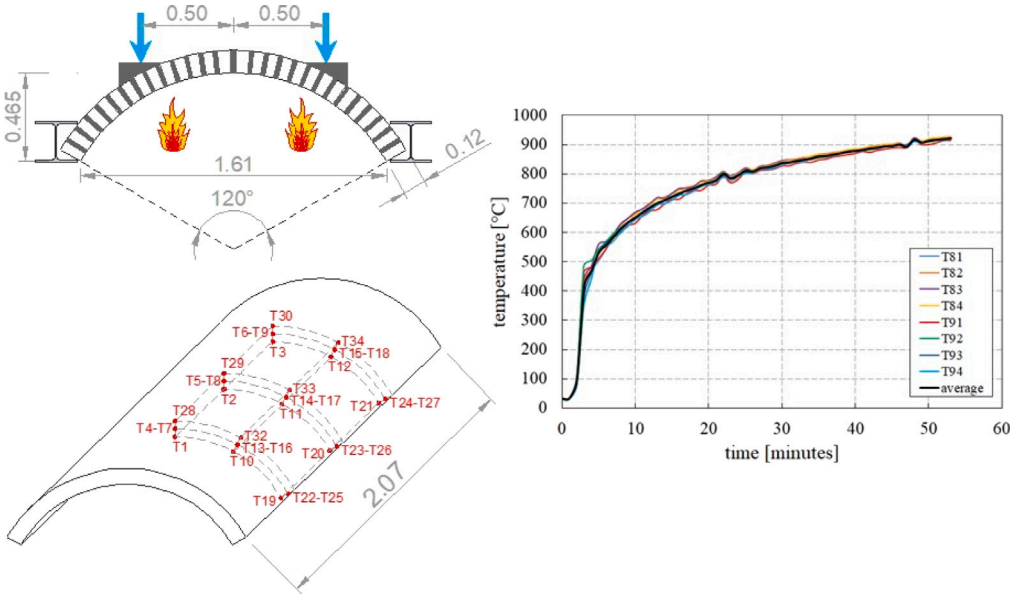

Fig. 7. Geometrical vault scheme (top left; measurement in meters) and thermocouple layout (lower left); air temperature recorded during the fire test in the oven (right).

radial displacement (top) and the crushing strain component (bottom) calculated analytically (continuous red line) and numerically (black bold points) are compared in Fig. 6, confirming that the solutions overlap also in terms of the radius of transition $r_c = 1.83$m. The comparison with the case of temperature independent compressive strength (Section 3.1) highlights how a maximum reduction of 15% of σ^c leads to an increase in the crushed area of 17% and a displacement increment of approximately 40%. Finally, using the *masonry-like* model implies a 96% rise in radial displacement compared to the linear elastic case.

4. A real case study

The constitutive equation outlined in Section 2 is here applied to analyse the behaviour of a real case study consisting of a barrel masonry vault (Fig. 7) tested in fire conditions by Vigili del Fuoco [14]. The vault has span length = 1.61 m, intrados radius = 0.93 m (0.465 m rise), thickness = 0.12 m and length = 2.070 m. Bricks of $55 \times 120 \times 250$ mm^3 and premixed cement-lime-based mortar were used for building the vault. In order to represent the backfill, two concentrated loads were symmetrically applied on two concrete curbs at a 0.5 m distance from the keystone. During the fire test, the temperature of the extrados, intrados and inside the vault were measured using 34 thermocouples placed according to the layout shown in Fig. 7. Additional thermocouples in the oven were allowed to monitor the air temperature in real time. The fire test was interrupted after 52 min, although neither collapses nor spalling occurred in the vault. The thermo-mechanical analysis, carried out by the NOSA-ITACA code, is here performed assuming that the displacement gradient, thermal expansion and its derivative with respect to temperature, strain rate and temperature rate are small so that the thermoelastic equilibrium equations governing the problem are uncoupled and can be integrated separately [27]. The thermal analysis and its results are shown in Section 4.1, while Section 4.2 analyses the vault's mechanical behaviour under the temperature gradient and the external static loads applied to the vault extrados.

4.1. Thermal analysis of the masonry vault.

The purpose of this subsection is to show that it is possible to obtain the temperature field measured in the vault during the experimental test [14], following the guidelines in Eurocode Part $1-2$ [36] and employing some parameter values recovered from the literature. During the test, the environmental temperature in the oven increased following the trend reported in Fig. 7, where the black line represents the mean temperature value recorded by the thermocouples placed in the oven. According to the Eurocode, the net flux heat $\dot{h}_{\text{net}}$ on the surface of a structural element exposed to fire can be determined by considering heat transfer by convection and radiation as:

$$\dot{h}_{\text{net}} = \dot{h}_{\text{net,c}} + \dot{h}_{\text{net,r}} \tag{53}$$

The net convective heat flux $\dot{h}_{\text{net,c}}$ and the net radiative heat flux component per unit surface area $\dot{h}_{\text{net,r}}$ are determined by:

$$\begin{aligned} \dot{h}_{\text{net,c}} &= \alpha_{\text{c}}(\vartheta_{\text{g}} - \vartheta_{\text{m}}) \\ \dot{h}_{\text{net,r}} &= \phi\varepsilon_{\text{m}}\varepsilon_{\text{f}}\sigma[(\vartheta_{\text{r}} + 273)^4 - (\vartheta_{\text{m}} + 273)^4] \end{aligned} \tag{54}$$

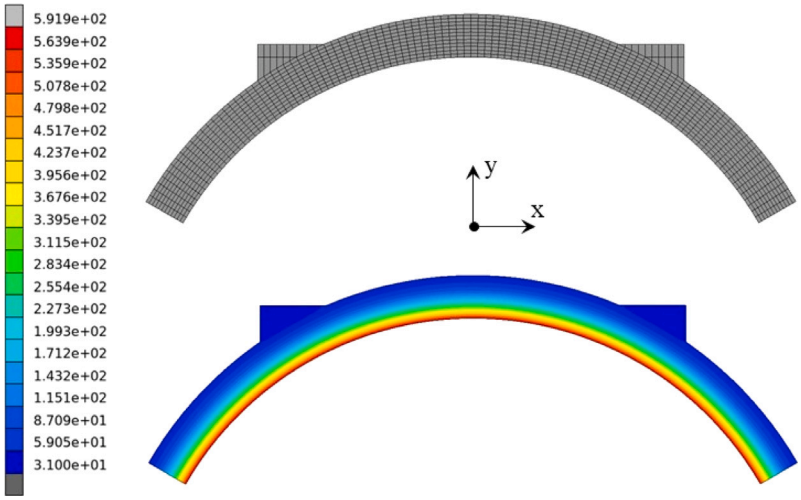

Fig. 8. Vault mesh (top) and absolute temperature field obtained by thermal analysis (bottom).

where: α_c is the coefficient of heat transfer by convection; ϑ_g and ϑ_m are the gas temperature in the vicinity of the fire exposed member and the surface temperature of the structural element; $\phi, \varepsilon_f, \varepsilon_m$ and σ are the configuration factor, the surface emissivity of the member, the emissivity of the fire and the Stephan Boltzman constant; ϑ_r is the effective radiation temperature of the fire environment [36]. The transient thermal analysis of the vault is performed by building a continuum FE model (Fig. 8) consisting of 1280 4-node isoparametric plane elements with linear shape functions (element 11 of NOSA-ITACA library) for a total of 1397 nodes and 1397 degrees of freedom and assuming the following temperature independent material properties: thermal conductivity 1 W/mK [37]; specific heat for unit mass 1000 J/kgK [38]; emissivity, 1.0; mass density 1720 kg/m^3 [14] and initial temperature 31 °C [14]. As boundary conditions a distributed flux $\dot{h}_{net,c}$ is applied to the vault's extrados assuming $\alpha_c = 9$ W/m^{2}K [36] and $\vartheta_g = 31$ °C while for the intrados surface the distributed flux expressed by (53) is used considering $\alpha_c = 25$ W/m^{2}K [36], ϑ_g equal to the mean value of temperature recorded during the fire test and neglecting $\dot{h}_{net,r}$ (in the absence of information on ϑ_r). Fig. 9 compares the experimental temperature histories and their numerical counterpars. In each chart, the grey lines represent the temperature increment recorded by each thermocouple, the black line their mean value and the red line the numerical result. Chart (a) is related to the thermocouples placed at the vault intrados, (b) and (c) refers to the thermocouples five and seven centimeters away, respectively, from the intrados and (d) is related to the thermocouples positioned at extrados. It is possible to notice the similarity of the experimental and numerical temperature trend at intrados and extrados with a maximum relative error of 3.8% (maximum experimental increment temperature 582 °C versus 560 °C numerical) at the intrados and 12.0% (maximum experimental increment temperature 27 °C versus 24 °C numerical) at the extrados. As regards the temperature trend inside the vault, the difference between the experimental and numerical data could be traced back to sensors malfunctioning or material non-linear behaviour not considered in the analysis.

4.2. Mechanical analysis of the masonry vault

The temperature field achieved by the previous thermal analysis is here applied to the FE model of the vault made of 1280 4-node isoparametric plane strain elements with linear shape functions (element 6 of NOSA-ITACA library) for a total of 1397 nodes and 2794 degrees of freedom. Together with the temperature, the self-weight of the vault and two concentrated loads equal to 8770 N each, and applied to the extrados of the concrete curbs, are also considered as acting on the model. The analysis is run assuming the vault clamped at the two ends and modelling the concrete as a linear elastic material characterised by an elastic modulus of 25 GPa, a Poisson's ratio equal to 0.2, a thermal expansion coefficient $\alpha = 10^{-5}(°C)^{-1}$ and a mass density of 2400 kg/m^3. The vault is modelled as a masonry-like material with zero tensile strength and temperature dependent compressive strength as reported in the Table 1, inspired by [12]:

For the other mechanical characteristics, the following values are assumed [39]:

$$\begin{aligned} &E = 4.0 \times 10^9 \text{ Pa}, \\ &\nu = 0.2, \\ &\alpha = 2.5 \times 10^{-6}(°C)^{-1}, \\ &\rho = 1720 \text{ kg/m}^3 \end{aligned} \tag{55}$$

Fig. 10 shows, at reference temperature ϑ_0 and at the end of the numerical simulation, the minimum eigenvalues of the stress tensor (top), maximum eigenvalues of the fracture strain tensor (middle) and lines of thrust (bottom) obtained from the integration,

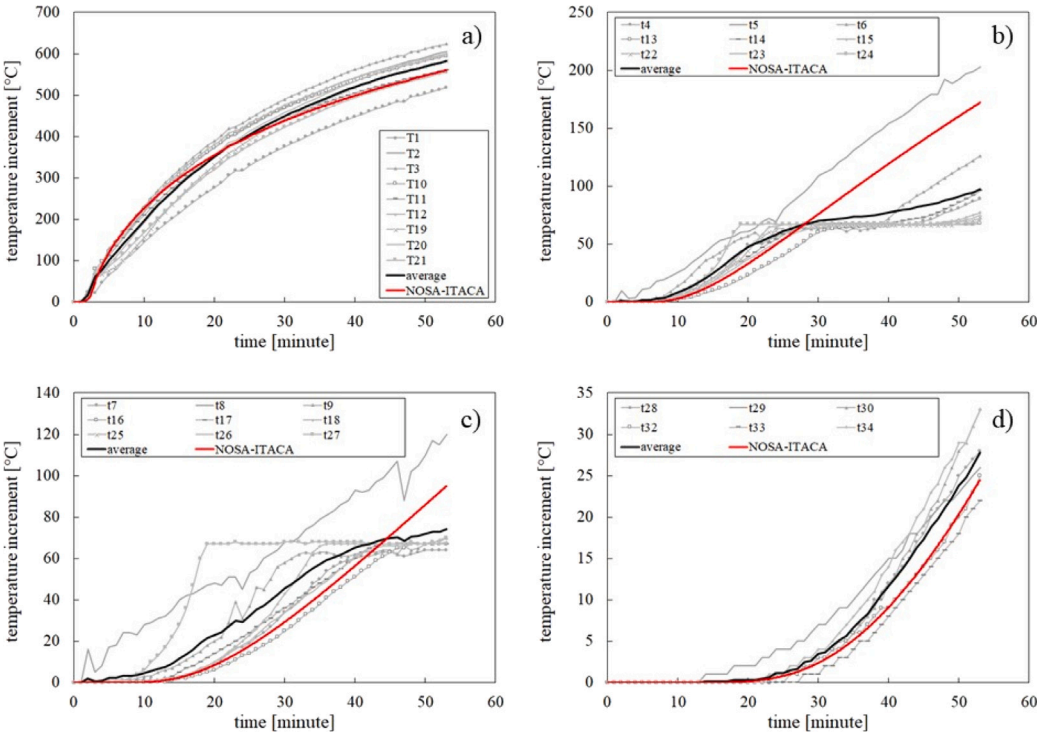

Fig. 9. Comparison between the temperature increment measured during the experimental test and the numerical counterpart.

Table 1
Compressive strength versus temperature.

ϑ [°C]	σ^c [10^6 Pa]
0	2.500
20	2.500
100	2.500
200	2.375
400	2.125
600	1.975
800	1.975

on several sections, of the circumferential stress. At ϑ_0, the minimum value of stress is far from the maximum compressive strength of the masonry, and this is confirmed by the fact that the thrust line is well contained within the vault thickness. In particular, it is possible to note four compressed struts due to the particular load condition represented by the applied concentrated loads equal to about the vault weight. Microfracture strains, such as those shown in the Figure, correspond to the stress field resulting from the masonry zero tensile strength hypothesis. When the intrados reaches the maximum temperature, the distribution of the minimum eigenvalues of the stress tensor is almost uniform, (Fig. 10) showing a higher value (approximately constant) at the intrados caused by the hindered expansion of the structure attributable to the boundary conditions. It is necessary to highlight that, in this case, the colour map associated with the stress field is intentionally limited to the value of -10^6 Pa to make the Figure more readable. In reality, at the vault ends, the maximum compressive strength of masonry is reached with the rise of local crushed areas, as shown in Fig. 12. About the thrust line, it moved towards the intrados of the vault and is characterised by constant eccentricity values; at the keystone it is almost tangential to the intrados which corresponds a concentration of fracture strains along the entire height of the section. Fig. 11 compares the experimental crack pattern with the numerical counterpart; the model can catch the fracture distribution very well also in terms of magnitude, with the keystone cracks deeper and more pronounced than the longitudinal fracture at the intrados.

Fig. 12(a,b) shows the time history of the minimum eigenvalues of the stress tensor at the interlock section intrados and extrados (points P1 and P2, respectively). After five minutes, the material at point P1 shows a nonlinear behaviour, until the end of the process, with the corresponding formation of crushing strains (Fig. 12c); the crushed area is limited to a small portion of the section as shown by the time history of P2 that reveals a linear elastic behaviour (Fig. 12b). Point P3 in the Figure, three centimeters from the intrados, represents the crossing point between the crushed and no-crushed zone. Fig. 12d outlines the time history of the maximum eigenvalues of the fracture strain for points P3 and P4; in this case, cracks grow up only a few minutes after the start of fire exposure.

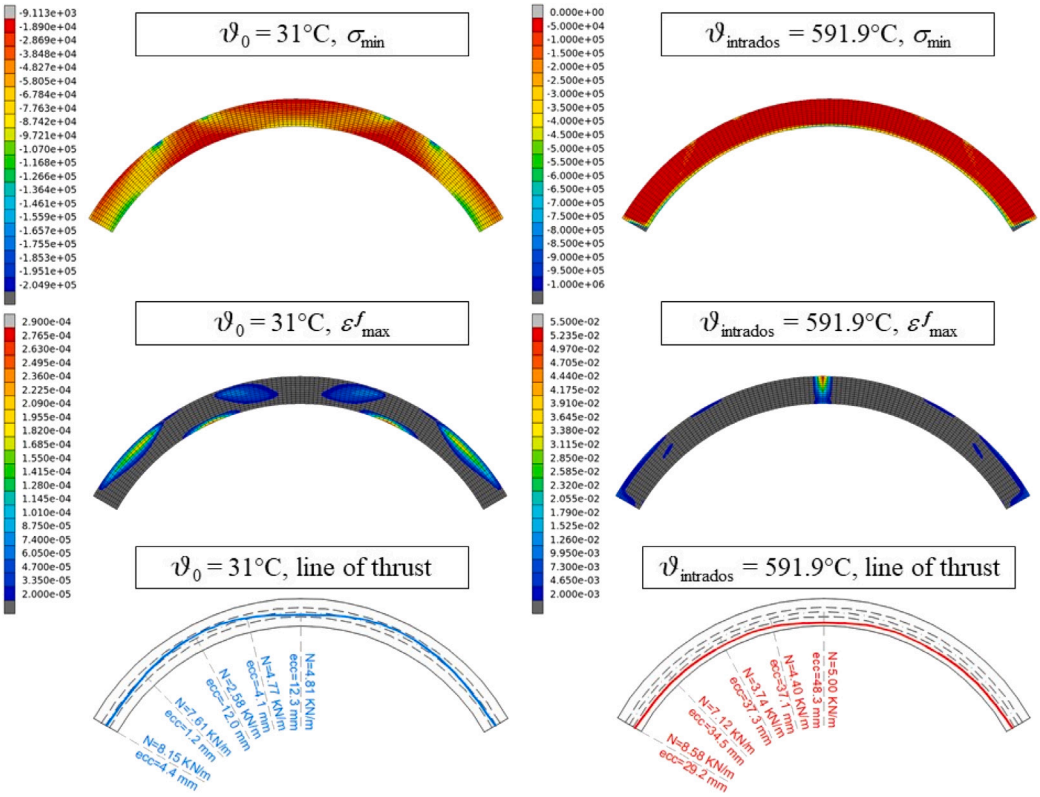

Fig. 10. Minimum eigenvalues of the stress tensor (top) at reference and final temperature; maximum eigenvalues of the fracture strain tensor (middle) at reference and final temperature; line of thrust (bottom) at reference and final temperature.

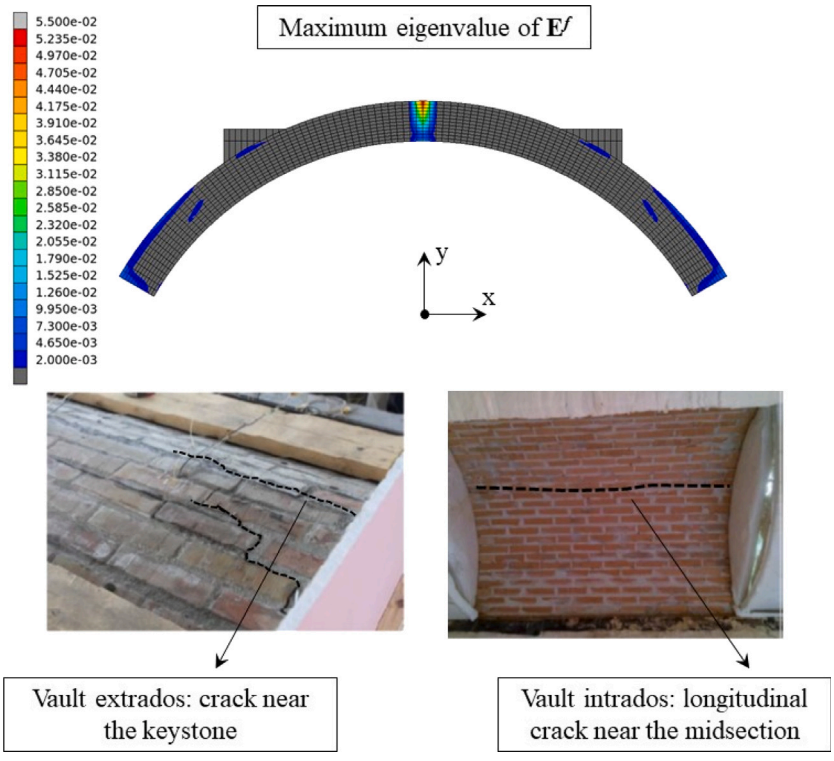

Fig. 11. Maximum eigenvalue of the fracture strain tensor (top); crack detected at the end of fire test (bottom).

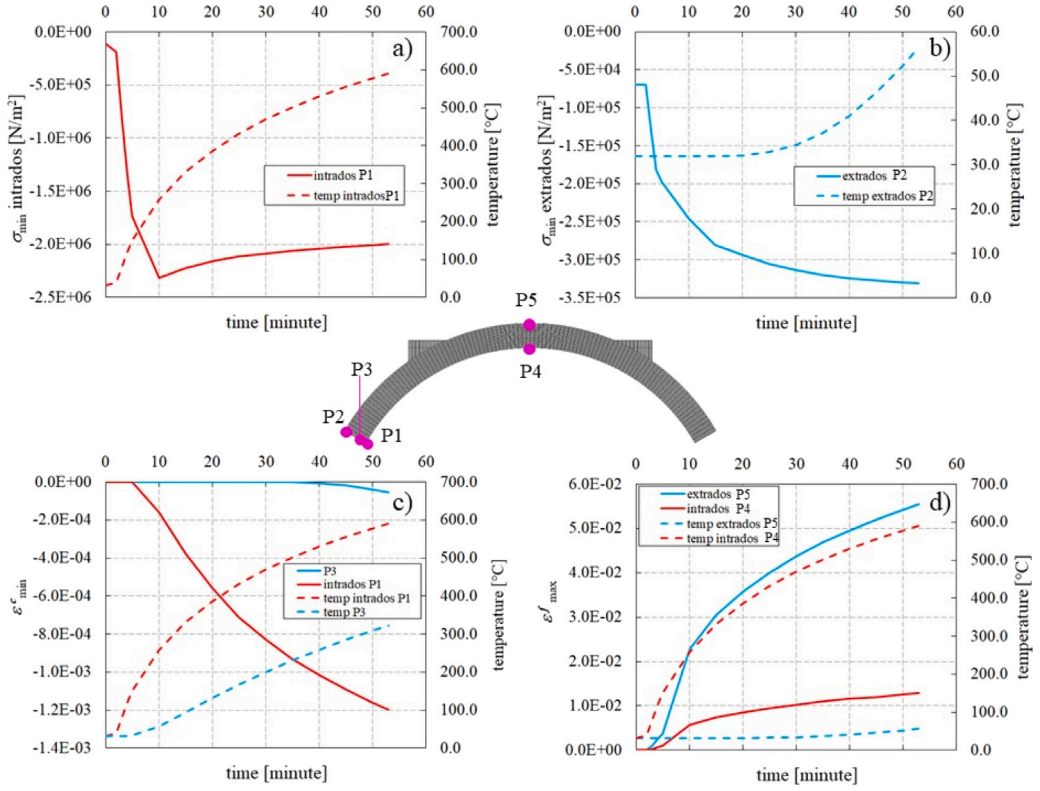

Fig. 12. Time history of: the minimum eigenvalues of the stress tensor at the interlock section intrados (a) and extrados (b); the minimum eigenvalues of the crushing strain tensor at the interlock section (c); the maximum eigenvalues of the fracture strain tensor at the keystone (d).

Finally, during the experimental test, the keystone displacement was measured using an LVDT; the value is 4.46 mm versus 4.64 mm obtained from the numerical model.

5. Conclusions

The present paper investigated the possibility of applying the constitutive equation of no-tension material to analyse the mechanical behaviour of masonry structures in fire and post-fire conditions. For this purpose, the equation describing *masonry-like* materials under non-isothermal conditions is generalised to consider the low tensile strength and bounded compressive strength of masonry, including temperature dependence. The constitutive equation is also implemented in NOSA-ITACA, a freeware finite element (FE) software developed in-house by ISTI-CNR devoted to analysing and calibrating the mechanical behaviours of historic masonry structures. Thereafter, the explicit solution to the equilibrium problem of a circular ring subjected to uniform radial pressures acting on the boundaries and to a stationary temperature field is calculated, modelling the constituent material as a *masonry-like* material with null tensile strength and bounded compressive strength temperature independent and dependent, resp. The ring is modelled by the FE code, and the comparison between the explicit solution and the numerical results (in terms of stress tensor components, crushing strain tensor components and displacements) shows a perfect overlapping. Then, the code is used to analyse the thermo-mechanical behaviour of a real case study consisting of a barrel masonry vault tested, in fire conditions, by Vigili del Fuoco. Assuming suitable hypotheses, the equations governing the thermo-mechanical equilibrium problem are uncoupled, so it is possible to perform a thermal analysis followed by a mechanical analysis applying the temperature field achieved to the FE vault. Both analyses are performed by NOSA-ITACA, assuming for masonry a zero tensile strength and temperature dependent bounded compressive strength. For simplicity, and due to a lack of information about the mechanical properties of the constituent material, all the other parameters necessary for the analyses were assumed temperature-independent, and their values were taken from the literature. The numerical results of the thermal analysis, in terms of temperature increments, are in good agreement with experimental ones measured at the vault intrados and extrados. However, the internal measurements show a deviation, likely attributable to sensor malfunctioning or non-linear behaviour of materials not considered in the numerical analysis. With respect to the mechanical analysis, first, it is noted that the masonry nonlinear tensile behaviour influences the structure's response more than the nonlinearity in compression, which affects only small areas of end sections of the vault. Furthermore, the model is able to catch very well the cracks patterns that occurs in the vaults, both in terms of location and magnitude. Finally, a comparison between the vault keystone experimental displacement, and the numerical counterpart shows a relative percentage error of 4%. The use of the

constitutive equation proposed, whose application requires the knowledge of only a few material mechanical characteristics, seems, therefore, suitable for the historic masonry buildings' structural safety analysis for which generally the knowledge of the materials mechanical properties is limited and can only be estimated by non-destructive in situ tests. Further investigations are necessary to validate the model, highlight its strengths and weaknesses and gather suggestions on improvements and changes. Future works will include: (i) execution of experimental campaigns to characterise the thermo-mechanical behaviour of masonry specimens; (ii) to study, from the experimental point of view, the response of curvilinear masonry elements in fire and post-fire conditions; (iii) the ability to perform coupled thermo-mechanical analyses with the NOSA-ITACA code.

CRediT authorship contribution statement

Daniele Pellegrini: Writing – review & editing, Writing – original draft, Validation, Supervision, Software, Methodology, Investigation, Formal analysis, Data curation, Conceptualization.

Declaration of competing interest

The authors declare that they have no known competing financial interests or personal relationships that could have appeared to influence the work reported in this paper.

Data availability

Data will be made available on request.

Acknowledgements

This research has been supported by the Italian National Research Council within the call Progetti di Ricerca @CNR, 2022–2024 (Revolution Project- open-source platform oriented toward digital twins: 3d digitisation techniques, vibration monitoring and finite element models for evaluating the conservation status of historical buildings and civil infrastructures). This support is gratefully acknowledged.

References

[1] Fulvio Parisi, Nicola Augenti, Earthquake damages to cultural heritage constructions and simplified assessment of artworks, Eng. Fail. Anal. 34 (2013) 735–760.
[2] Miloš F. Drdáckỳ, Flood damage to historic buildings and structures, J. Perform. Constru. Facil. 24 (5) (2010) 439–445.
[3] Gianni Bartoli, Michele Betti, Maria Girardi, Cristina Padovani, Daniele Pellegrini, Giacomo Zini, Dynamic monitoring of a tunnel-like masonry structure using wireless sensor networks, Proc. Inst. Civ. Eng.-Struct. Build. (2022) 1–12.
[4] E. Garcia-Castillo, I. Paya-Zaforteza, A. Hospitaler, Fire in heritage and historic buildings, a major challenge for the 21st century, Dev. Built Environ. (2022) 100102.
[5] P.D. Gkournelos, T.C. Triantafillou, D.A. Bournas, Seismic upgrading of existing masonry structures: A state-of-the-art review, Soil Dyn. Earthq. Eng. 161 (2022) 107428.
[6] Serena Cattari, Bruno Calderoni, Ivo Caliò, Guido Camata, Stefano de Miranda, Guido Magenes, Gabriele Milani, Anna Saetta, Nonlinear modeling of the seismic response of masonry structures: critical review and open issues towards engineering practice, Bull. Earthq. Eng. 20 (4) (2022) 1939–1997.
[7] British Standard, Eurocode 6–design of masonry structures, Br. Stand. Inst. London (2005) (2005).
[8] Salvatore Russo, Francesca Sciarretta, Masonry exposed to high temperatures: Mechanical behaviour and properties–An overview, Fire Saf. J. 55 (2013) 69–86.
[9] Marco Andreini, Mauro Caciolai, Saverio La Mendola, Lamberto Mazziotti, Mauro Sassu, Mechanical behavior of masonry materials at high temperatures, Fire Mater. 39 (1) (2015) 41–57.
[10] Josipa Bošnjak, Serena Gambarelli, Akanshu Sharma, Amra Mešković, Experimental and numerical studies on masonry after exposure to elevated temperatures, Constr. Build. Mater. 230 (2020) 116926.
[11] Jin Zhang, Hao Ma, Cheng Li, Qingfeng Xu, Weibin Li, Experimental study on seismic performance of fire-exposed perforated brick masonry wall, Constr. Build. Mater. 180 (2018) 77–91.
[12] Aditya Daware, M.Z. Naser, Fire performance of masonry under various testing methods, Constr. Build. Mater. 289 (2021) 123183.
[13] Alessandro P. Fantilli, Nicholas S. Burello, Masonry arches and vaults under fire, J. Build. Eng. 56 (2022) 104740.
[14] DCPSP Vigili del Fuoco, Experimental fire test on a barrel vault (in Italian), 2015.
[15] Ali Nadjai, M. O. garra, F. Ali, Finite element modelling of compartment masonry walls in fire, Comput. Struct. 81 (18–19) (2003) 1923–1930.
[16] Wasim Khaliq, Muhammad Farrukh Bashir, High temperature mechanical and material properties of burnt masonry bricks, Mater. Struct. 49 (2016) 5195–5208.
[17] S. Russo, F. Sciarretta, Experimental and theoretical investigation on masonry after high temperature exposure, Exp. Mech. 52 (2012) 341–359.
[18] Fabian Rene Ruvalcaba Ayala, Mechanical Properties and Structural Behaviour of Masonry At Elevated Temperatures, The University of Manchester (United Kingdom), 2011.
[19] Zhao Xiao, Tung-Chai Ling, Chi-Sun Poon, Shi-Cong Kou, Qingyuan Wang, Runqiu Huang, Properties of partition wall blocks prepared with high percentages of recycled clay brick after exposure to elevated temperatures, Constr. Build. Mater. 49 (2013) 56–61.
[20] Thê-Duong Nguyen, Fekri Meftah, Behavior of hollow clay brick masonry walls during fire. Part 2: 3D finite element modeling and spalling assessment, Fire Saf. J. 66 (2014) 35–45.
[21] Salvatore Russo, Francesca Sciarretta, Numerical investigation on the residual behaviour of masonry walls damaged by fire exposure, Key Eng. Mater. 624 (2014) 230–237.
[22] S. Russo, F. Sciarretta, Numeric research on the mechanical properties of different masonry units during and after fire, in: Brick and Block Masonry, CRC Press, 2016, pp. 999–1006.

[23] P Ravi Prakash, Miguel Azenha, João M Pereira, Paulo B Lourenço, Finite element based micro modelling of masonry walls subjected to fire exposure: Framework validation and structural implications, Eng. Struct. 213 (2020) 110545.
[24] Elodie Donval, Duc Toan Pham, Ghazi Hassen, Patrick de Buhan, Didier Pallix, Determination of the deformed shape of a masonry wall exposed to fire loading by a homogenization method, in: IOP Conference Series: Materials Science and Engineering, vol. 1203, (3) IOP Publishing, 2021, 032076.
[25] Elodie Donval, Duc Toan Pham, Ghazi Hassen, Patrick de Buhan, Didier Pallix, A numerical homogenization method for the determination of the thermal bowing of a masonry wall exposed to fire: Application to natural stone masonry, Eng. Struct. 266 (2022) 114541.
[26] T Parent, M Brocato, A-S Colas, N Domede, F Dubois, D Garnier, A Gros, J-C Mindeguia, S Morel, P Morenon, et al., A multi-model structural analysis of the vaults of notre-dame de Paris cathedral after the 2019 fire and a proposal for a hybrid model merging continuum and discrete approaches, J. Cult. Herit. (2023).
[27] Massimiliano Lucchesi, Cristina Padovani, Giuseppe Pasquinelli, Thermodynamics of no-tension materials, Int. J. Solids Struct. 37 (45) (2000) 6581–6604.
[28] Cristina Padovani, Giuseppe Pasquinelli, Nicola Zani, A numerical method for solving equilibrium problems of no-tension solids subjected to thermal loads, Comput. Methods Appl. Mech. Engrg. 190 (1–2) (2000) 55–73.
[29] Gianpietro Del Piero, Constitutive equation and compatibility of the external loads for linear elastic masonry-like materials, Meccanica 24 (1989) 150–162.
[30] Massimiliano Lucchesi, Cristina Padovani, Giuseppe Pasquinelli, Nicola Zani, Masonry Constructions: Mechanical Models and Numerical Applications, Springer Science & Business Media, 2008.
[31] Maria Girardi, Cristina Padovani, Daniele Pellegrini, Margherita Porcelli, Leonardo Robol, Numerical modelling of historical masonry structures with the finite element code NOSA-ITACA, in: INdAM Workshop: Mathematical Modeling and Analysis of Degradation and Restoration in Cultural Heritage, Springer, 2021, pp. 133–152.
[32] Daniele Pellegrini, Pre-and post-diction simulation of the seismic response of a masonry cross vault tested on a shaking table, Int. J. Archit. Herit. (2023) 1–21.
[33] D Pellegrini, A Barontini, M Girardi, PB Lourenço, MG Masciotta, N Mendes, C Padovani, LF Ramos, Effects of temperature variations on the modal properties of masonry structures: An experimental-based numerical modelling approach, in: Structures, vol. 53, Elsevier, 2023, pp. 595–613.
[34] S. Timoshenko, J.N. Goodier, Theory of Elasticity, Mc GRAW-Hill. Book. Company. Inc., New York, 1951.
[35] Cristina Padovani, No-tension solids in the presence of thermal expansion: An explicit solution, Meccanica 31 (1996) 687–703.
[36] Eurocode 1: Actions on structures – Part 1–2: General actions – Actions on structures exposed to fire.
[37] Alfredo Llorente-Alvarez, Maria Soledad Camino-Olea, Alejandro Cabeza-Prieto, Maria Paz Saez-Perez, Maria Ascensión Rodríguez-Esteban, The thermal conductivity of the masonry of handmade brick cultural heritage with respect to density and humidity, J. Cult. Herit. 53 (2022) 212–219.
[38] L Krishnaraj, R Niranjan, G Prem Kumar, Rajendran Senthil Kumar, Numerical and experimental investigation on mechanical and thermal behaviour of brick masonry: An efficient consumption of ultrafine fly ash, Constr. Build. Mater. 253 (2020) 119232.
[39] B. Ghiassi, A.T. Vermelfoort, P.B. Lourenço, Chapter 7 - masonry mechanical properties, in: Bahman Ghiassi, Gabriele Milani (Eds.), Numerical Modeling of Masonry and Historical Structures, in: Woodhead Publishing Series in Civil and Structural Engineering, Woodhead Publishing, ISBN: 978-0-08-102439-3, 2019, pp. 239–261.